# The impact of the 2018 Lombok earthquake sequence, Indonesia on the unrest Rinjani-Samalas volcanic complex inferred from the time-dependent seismic and volcanic source models

**Siyuan Zhao**[1], Simon McClusky[1,2], Meghan Miller[1], and Phil Cummins[1,2]

- [1]The Australian National University, Research School of Earth Sciences, Australia (Siyuan.Zhao@anu.edu.au)
- [2]Geoscience Australia, Canberra, ACT, Australia

## Introduction

In 2018, four deadly (Mw 6.2-6.9) earthquakes struck the north coast of Lombok Island on 28 July, 5 August, and 19 August, distributed between the Flores back-arc thrust and the Rinjani-Samalas volcanic complex. The fault geometries and slip distributions of these earthquakes are modelled in this study by inverting the co-seismic deformation imaged using an interferometric analysis of Sentinel-1 synthetic aperture radar measurements (InSAR), based on rectangular dislocations embedded in a multi-layered elastic half-space. Our best-fit co-seismic slip model suggests the estimated maximum fault slip of 1.3 m, 2.2 m, and 2.5 m for the mainshocks from July to August, located at the depth of 9.6 km, 13.6 km, and 22.2 km, respectively. We performed an unsupervised learning method (ST-DBSCAN) to cluster the relocated aftershocks so that we can identify the source of each aftershock. The clustered aftershocks are primarily distributed in the areas with increased Coulomb stress and are less abundant in the maximum slip patch on the three rupture faults, indicating high consistency with our estimated co-seismic slip model. We use an InSAR time-series consisting of 662 descending and 371 ascending Sentinal-1 interferograms to investigate the time-dependent inflation and deflation signals generated by the 2015, 2016 eruptions and 2018 earthquake Sequence. We use a combined model that simulates the viscoelastic relaxation and afterslip simultaneously to explain the two-years post-seismic behaviour, which suggests a Maxwell viscosity of $1x10^{18}$ Pa s for both lower crust and asthenosphere, and it reveals that the maximum of the accumulative afterslip within two years is ~0.7 m, along the northwestward up-dip continuation of the co-seismic rupture area. The Coulomb stress change modelling based on the coseismic and two-year cumulative post-seismic rupture models indicates about 0.5 MPa of extensional stress change at 5 to 15 km of depth and 1 Mpa extensional stress change at 15 to 25 km of depth around the Barujari Crater region, respectively, which may promote the opening of the magma conduit.

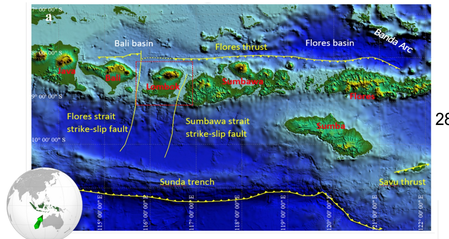


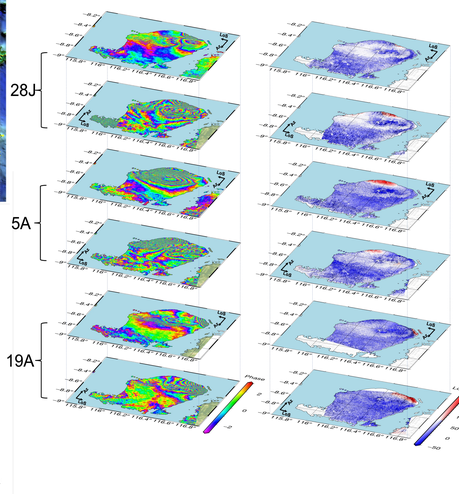


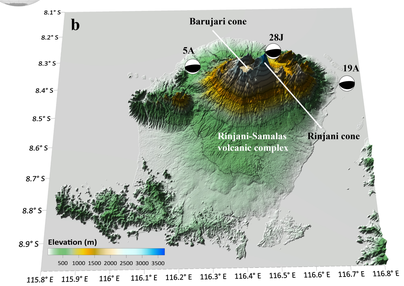


## Aftershock analysis

In this study, the three major events of the 2018 Lombok earthquake sequence occurred within only one month, and the estimated rupture area are spatially close to each other, within only 12 km at the nearest place, hence, the origin of the aftershocks is hard to be clarified spatially and temporally. We applied the ST-DBSCAN clustering algorithm based on Birant and Kut (2007) to classify the Sasmi et al. (2020) aftershocks on the similarity of their spatiotemporal attributes, including longitude, latitude, depth and origin time. It allows us to discover the clusters of the spatial-temporal clusters in the aftershock dataset. The K-Nearest Neighbours (KNN) method was used to determine the parameters (Birant and Kut 2007). We adopt the modified Omori–Utsu law (Utsu and Ogata 1995), which describes the occurrence rate of aftershocks n(t), to test our clustering results.

Our clustered aftershocks show higher correspondence to the calculated Coulomb stress change. Nearly all the clustered off-fault aftershocks appear to fall in the Coulomb stress increase regions, while for the unclustered events, numbers of earthquakes are distributed irregularly in the stress decrease regions (right c-f), which indicates that the aftershock clustering did identify the source of most aftershocks.

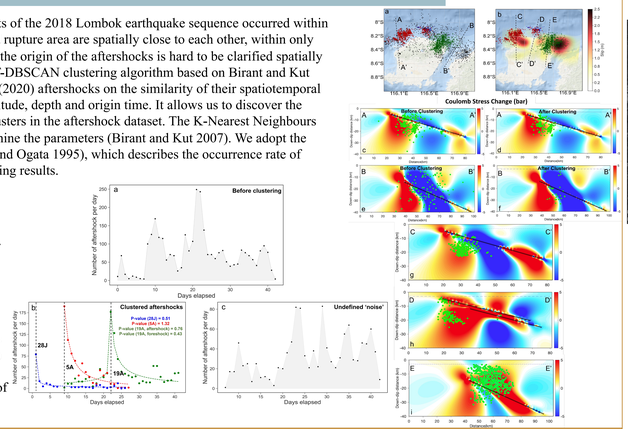


## Time-dependent afterslip & viscoelastic relaxation modelling

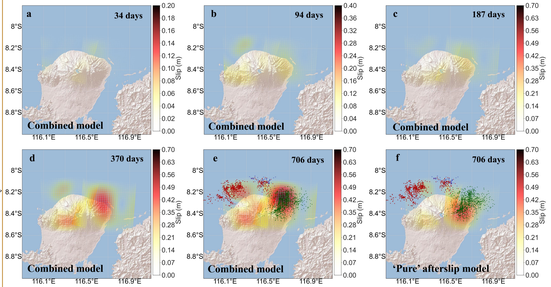


As the cumulative afterslip can also generate the viscoelastic relaxation, leading to an overestimation of the afterslip and an inaccurate rupture behaviour interpretation, we generate a combined model that estimate both post-seismic mechanisms simultaneously.

The combined model suggests that the post-seismic response through the 19A event was dominated by an afterslip along the northwestward up-dip continuation of the coseismic rupture rather than the south-westward down-dip continuation displayed in the 'pure' afterslip model, revealing that in the later period, correct the deep-source induced postseismic deformation results from the viscoelastic relaxation make the estimated afterslip more clearly at the shallow near-field region.

## InSAR time-series analysis

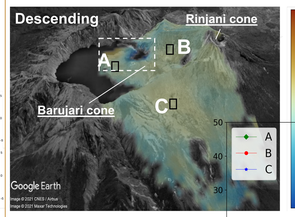


In 1257, a catastrophic eruption occurred on the former Mt Samalas, leading to the caldera collapse, with volcanic activity shifting to Barujari volcano on the caldera rim. To quantify the volcano deformation before and after the earthquake sequence, we extend the time range of our InSAR time-series analysis to the year 2014, covering the two eruptions occurred in the 2015 and 2016.

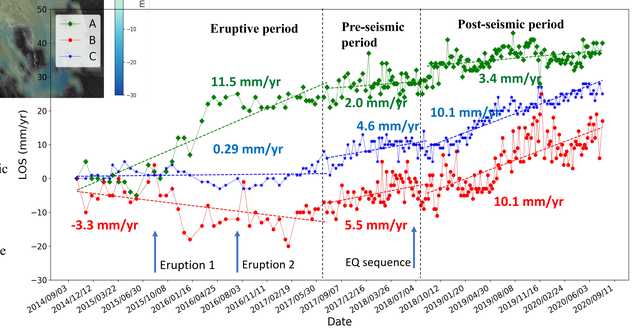


The variation of the displacement rates of these three areas exhibit similar patterns during the pre-seismic and post-seismic periods, however, during the eruptive period, area A near Barujari shows a relatively large inflation rate. This co-eruptive sudden inflation at area A indicates the existence of an eruptive fissure, and we can clearly see the local co-eruptive signal near this possible eruptive fissure.

In order to extract all the spatial patterns of deformation embedded in the InSAR time series (longer term and seasonal) and evaluate their evolution in time, we preform the T-mode PCA (Chaussard et al., 2014) , which is a statistically-based approach to extract the signals with maximum spatiotemporal coherence.

The PC1 eigenvector time series shows a decrease between 2014 and 2017and remains nearly constant during 2017–2020, indicating that the long-term deformation pattern was mostly limited to 2014–2017, associated with the two eruptions.

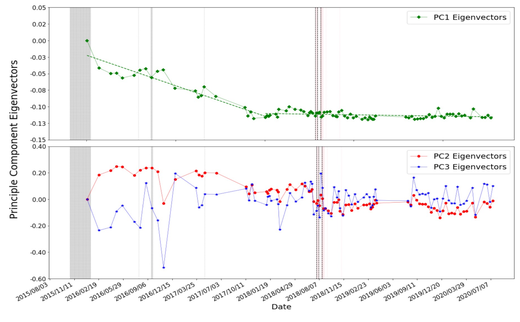


## Co-seismic slip distribution

The descending and ascending interferograms were inverted simultaneously by using the Geodetic Bayesian Inversion Software (GBIS) to estimate the fault geometry and uniform slip displacement (Bagnardi and Hooper 2018) and use the Steepest Descent Method (SDM; Wang et al. 2013) to detect the distribution of the slip along the fault plane. In this study, we used a nine-layer 1D velocity model derived from Salman et al. (2020). The influence of the topographic surface on inferred slip models was accounted for by using the receiver elevation correction method (Williams and Wadge 1998). During the inversion, the descending and ascending interferograms were weighted by their respective reference misfits as described in data (Smittarello et al. 2019).

Our distributed slip models suggest a peak slip of 1.3 m at a depth of 9.6 m for 28J. The direction of the slip on the rupture plane is northward. For the 5A event, the maximum displacement on the rupture plane is 2.2 m at a depth of 13.6 km; the slip is distributed from the depth of ~7 km to 18 km with the direction mainly to the north, and generally turns northwestward at the northwest part of the rupture plane. The slip distribution in 19A is characterized by a single asperity with the maximum slip reaching 2.5 m, located at a depth of 22.2 km. The slip direction is slightly towards the northwest at a depth ranging from 15 to 30 km.

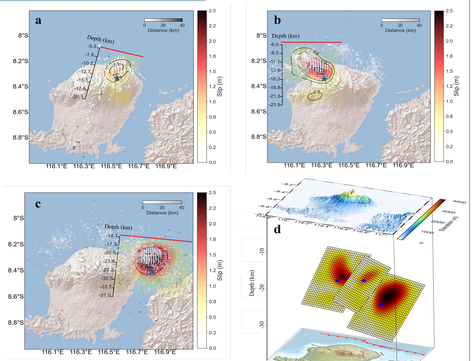


## Volcanic Source Modelling

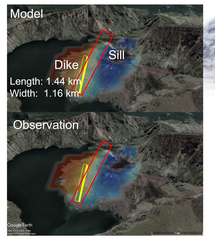


For the coeruptive signal surrounding the eruptive fissure, a uniform sill and dike combined model were generated. Our best-fit dike is nearly vertical, reaching a depth of up to 2 km below sea level, opening of 8.5 cm, and the sill is at the depth of 3.1 km, contracting of 40 cm.

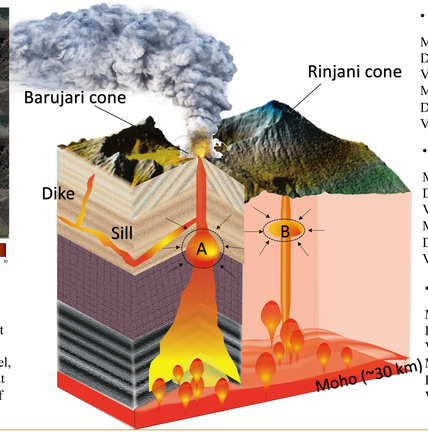


- **Eruptive period:**

Moji point source A:
Depth: ~3.9 km
Volume change: -3.0x$10^5$ $m^3$
Moji point source B:
Depth: ~3.5 km
Volume change: -2.3x$10^5$ $m^3$

- **Pre-seismic period:**

Moji point source A:
Depth: ~3.3 km
Volume change: 8.5x$10^4$ $m^3$
Moji point source B:
Depth: ~3.6km
Volume change: 7.2x$10^4$ $m^3$

- **Post-seismic period:**

Moji point source A:
Depth: ~5.0 km
Volume change: 9.4x$10^5$ $m^3$
Moji point source B:
Depth: ~3.6km
Volume change: 3.1x$10^5$ $m^3$

About 0.5 Mpa of extensional stress change between 5 and 15 km depth, and 1.0 Mpa compressional stress changes at greater depth (20 - 30 km) were estimated due to the mainshocks. These results suggest magmatic overpressure occurred at depth, with magma ascending into the opening shallow conduit. This magma ascent encourages the intrusion of a magma dike, and the compression occurring at the intermediate-lower crust facilitates sill development.

During the post-seismic periods, most of the positive Coulomb stress is concentrated within the depth of 15 to 25 km of the volcanic edifice, with the maximum value ~1 Mpa close to the magma conduit, and above 15 km, the normal stress changes drop to only ~0.1 Mpa at the magma conduit region, revealing the depressurization in the magma plumbing system.

**Normal stress change based on the co-seismic rupture model**

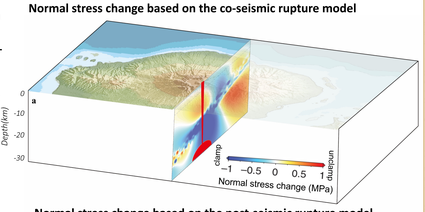


**Normal stress change based on the post-seismic rupture model**

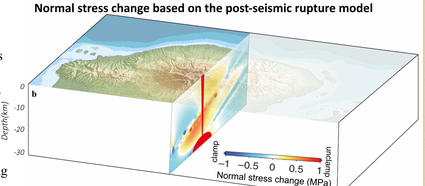


## References

Bagnardi, M., & Hooper, A. (2018). Inversion of surface deformation data for rapid estimates of source parameters and uncertainties: A Bayesian approach. *Geochemistry, Geophysics, Geosystems, 19*, 2194-2211.

Wang, R., Diao, F., & Hoechner, A. (2013). SDM-A geodetic inversion code incorporating with layered crust structure and curved fault geometry. In, *EGU General Assembly Conference Abstracts*.

Salman, R., Lindsey, E.O., Lythgoe, K.H., Bradley, K., Muzli, M., Yun, S.H., Chin, S.T., Tay, C.W., Costa, F., & Wei, S. (2020). Cascading Partial Rupture of the Flores Thrust during the 2018 Lombok Earthquake Sequence, Indonesia. *Seismological Research Letters*.

Williams, C.A., & Wadge, G. (1998). The effects of topography on magma chamber deformation models: Application to Mt. Etna and radar interferometry. Geophysical Research Letters, 25, 1549-1552.

Smittarello, D., Cayol, V., Pinel, V., Froger, J.-L., Peltier, A., & Damont, Q. (2019). Combining InSAR and GNSS to track magma transport at basaltic volcanoes. Remote Sensing, 11, 2236.

Birant, D., & Kut, A. (2007). ST-DBSCAN: An algorithm for clustering spatial–temporal data. Data & knowledge engineering, 60, 208-221.

Utsu, T., & Ogata, Y. (1995). The centenary of the Omori formula for a decay law of aftershock activity. Journal of Physics of the Earth, 43, 1-33.

Chaussard, E., Bürgmann, R., Shirzaei, M., Fielding, E.J., & Baker, B. (2014). Predictability of hydraulic head changes and characterization of aquifer-system and fault properties from InSAR-derived ground deformation. Journal of Geophysical Research: Solid Earth, 119, 6572-6590.

Wang, R., Lorenzo-Martín, F., & Roth, F. (2006). PSGRN/PSCMP—a new code for calculating co- and post-seismic deformation, geoid and gravity changes based on the viscoelastic-gravitational dislocation theory. Computers & Geosciences, 32(4), 527-541.